Titania−Carbon Nanocomposite Anodes for Lithium Ion Batteries—Effects of Confined Growth and Phase Synergism

Nicholas D. Petkovich, Benjamin E. Wilson, Stephen G. Rudisill, and Andreas Stein*

Department of Chemistry, University of Minnesota, 207 Pleasant Street SE, Minneapolis, Minnesota 55455, United States

S *Supporting Information*

ABSTRACT: As lithium-ion batteries (LIB) see increasing use in areas beyond consumer electronics, such as the transportation sector, research has been directed at improving LIBs to better suit these applications. Of particular interest are materials and methods to increase Li^+ capacity at various charge/discharge rates, to improve retention of Li^+ capacity from cycle-to-cycle, and to enhance various safety aspects of electrode synthesis, cell construction, and end use. This work focuses on the synthesis and testing of three-dimensionally ordered macroporous (3DOM) TiO_2/C LIB anode materials prepared using low toxicity precursors, including ammonium citratoperoxotitanate(IV) and sucrose, which provide high capacities for reversible Li^+ insertion/extraction. When the composites are pyrolyzed at 700 °C, the carbon phase restricts sintering of TiO_2 crystallites and keeps the size of these crystallites below 5 nm. Slightly larger crystallites are produced at higher temperatures, alongside a titanium oxycarbide phase. The composites exhibit excellent capacities as LIB anodes at low to moderate charge/discharge rates (in the window from 1 to 3 V vs Li/Li^+). Composites pyrolyzed at 700 °C retain over 200 mAh/g TiO_2 of capacity after 100 cycles at a C/2 rate (C = 335 mA/g), and do not suffer from extensive cycle-to-cycle capacity fading. A substantial improvement of overall capacities, especially at high rates, is attained by cycling the composite anodes in a wider voltage window (0.05 to 3 V vs Li/Li^+), which allows for Li^+ intercalation into carbon. At currents of 1500 mA/g of active material, over 200 mAh/g of capacity is retained. Other structural aspects of the composites are discussed, including how rutile TiO_2 is found in these composites at sizes below the thermodynamic stability limit in the pure phase.

KEYWORDS: titania, carbon, lithium-ion battery, nanocomposite, confined crystallization
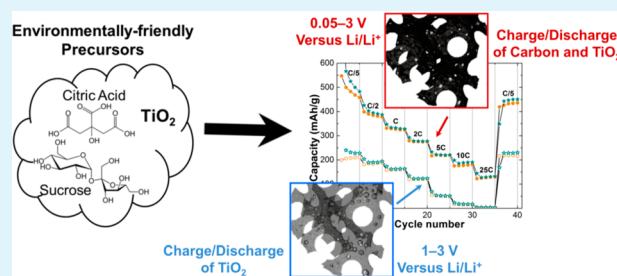
INTRODUCTION

In the early 1990s, the first lithium-ion batteries (LIB) were commercialized. Owing to their high energy density and attainable long cycle life, LIBs gradually displaced nickel−metal hydride batteries in personal electronic devices.[1] LIBs are now being developed and deployed as power sources for other applications, such as transportation and grid-scale storage.[2,3] Advances are still needed (especially for the transportation sector) to increase the higher energy densities of LIBs, enhance their ability to charge/discharge quickly, and improve their safety.[4] One method to accomplish these goals is to modify the composition and structure of the electrode materials. This paper focuses on two anode materials, TiO_2 and carbon, and a reduced-toxicity synthesis capable of generating electrodes with structural characteristics favorable for lithium storage.

Most commercially available LIBs that power consumer devices have a similar configuration. These batteries contain a carbon anode, a lithium cobalt oxide cathode, and a carbonate electrolyte with a dissolved lithium salt.[5] Although carbon is a popular anode material, it has some limitations that make it less favorable for transportation applications. Carbon anodes are operated at potentials near the Li/Li^+ couple, which lead to breakdown of the electrolyte, formation of a solid-electrolyte interface (SEI), and can eventually result in dangerous lithium plating on the anode surface.[6,7] When graphite is used as an anode material, capacities for Li^+ insertion/extraction decrease precipitously at high charge/discharge rates. Alternate lithium insertion materials have been explored to alleviate safety problems present in carbon systems, and to provide high power densities. Titanium dioxide has emerged as a potential candidate for several reasons: lithium insertion in TiO_2 occurs at a higher potential (~1.5−1.7 V vs Li/Li^+) that avoids plating, the material is minimally toxic and abundant, and TiO_2 can be charged and discharged rapidly without crippling losses to capacity.[8,9] However, satisfactory utilization of the capacity and rate performance of TiO_2 is only attainable by using nanoscale TiO_2, nanoporous TiO_2, and/or composites that contain TiO_2 and a secondary conductive phase.[8] In TiO_2-containing materials with controlled morphologies, it is possible to shorten diffusion lengths, to better accommodate volume changes, and to increase the area available for insertion/extraction reactions.[9−11] With composites, it is possible to greatly increase the electronic conductivity of the electrode material over that of

pure TiO_2.[12] Unfortunately, TiO_2 has a lower theoretical capacity for Li^+ storage than various allotropes of carbon.

To effectively use TiO_2 as an anode material, porous composites of TiO_2 and carbon have been synthesized using a combination of sol−gel chemistry and hard/soft templates.[13−21] Many composites simply use carbon as an inactive conductive additive. For instance, Zeng et al. filled an ordered mesoporous carbon material with TiO_2 crystallites and partially combusted the carbon phase.[19] This material contains a low fraction of carbon, and contains a favorable morphology for electron and lithium-ion conduction. Recently, it has been observed that high capacities can be obtained by cycling mesoporous TiO_2/C composites in a voltage window that allows for lithium intercalation and deintercalation to occur in the carbon phase.[16,18,22,23] Although cycling in an expanded voltage window erases some safety advantages, this allows TiO_2/C composite materials to attain higher capacities than either pure TiO_2 or C with similar structures.[16,22] At high rates, the composite anodes retain much greater capacities than what is possible for graphite anodes.[18] So far, soft-templated mesoporous materials have been primarily studied for TiO_2/C anodes cycled in an expanded voltage window.[16,18] Hard templates can offer better fidelity for replication (or inverse replication) of a porous structure, especially macroporous structures.[24] One versatile method for hard templating uses ordered arrays of spherical particles, colloidal crystals, as templates for the synthesis of negative replica structures with a bicontinuous network of pores and solid material.[25] These three-dimensionally ordered macroporous (3DOM) structures offer moderate surface areas for intercalation reactions, short diffusion lengths, and an interconnected pore structure that aids in electrolyte transport.[26] Researchers have successfully used 3DOM TiO_2 to fabricate anodes with good capacities and rate performance,[27,28] but little research has been conducted regarding 3DOM TiO_2/C composite anodes.[17] As a consequence, it is not known if 3DOM TiO_2/C electrodes can be cycled in a wide voltage window, so as to improve capacities for Li^+ insertion and extraction.

Many routes have been devised for the synthesis of carbon and TiO_2 composites that possess favorable electrochemical properties; however, few studies have specifically targeted means to minimize the toxicity of the synthesis precursors (via greener chemistries). Because an important motivation for the use of TiO_2 is to improve safety in batteries, it is logical to also consider the safety of syntheses for advanced electrode materials containing TiO_2. For instance, the introduction of amorphous carbon into a composite is commonly achieved using toxic organic molecules, such as phenol, formaldehyde, aniline, and furfural alcohol.[29,30] Other carbon sources, such as graphene and carbon nanotubes, present their own safety concerns that are still under intense investigation.[31,32] In addition, precursors used for the synthesis of TiO_2 are often toxic, such as the volatile $TiCl_4$, or require stabilization through the use of volatile and hazardous chelating agents.[17,33,34] Greener synthesis routes that use less dangerous precursors represent an important research direction for TiO_2 electrodes, including routes that produce materials with good capacity for lithium insertion and extraction.

This paper describes new syntheses of 3DOM TiO_2/C electrodes using a water-soluble, ammonium citratoperoxotitanate(IV) precursor for TiO_2 and different precursors (PF sol, sucrose, and citric acid) for amorphous carbon. In addition to being a greener synthesis pathway for

TiO_2/C, the 3DOM TiO_2/C electrodes contain nearly a 1:1 TiO_2 to carbon ratio (by weight) and are excellent candidate electrodes for cycling in a wide voltage window. A major focus of this work is an exploration on how the final pyrolysis temperature alters the structural and electrochemical properties of the composites. Another focus is the effect of changing the precursor from one that contains PF sol to a safer alternative that contains sucrose on the structure of these composite materials. Attention is also paid to how the precursor impacts the location and composition of the TiO_2 phase in the carbon matrix, a crucial factor in electrode performance. No matter which specific synthesis is used, the 3DOM TiO_2/C materials have a relatively high carbon content, which allows for high Li^+ insertion/extraction capacities at low rates in the voltage range from 1 to 3 V vs Li/Li^+. However, the capacity of these composites at high rates is curtailed. As alluded to earlier, to utilize both components of the composites and improve capacities, cycling was also conducted in an extended voltage range (0.05−3 V vs Li/Li^+). These experiments have led to further evidence that composites of TiO_2 and C provide a considerably higher lithium-ion capacity than similarly structured materials containing only carbon. Furthermore, this boosted capacity can be obtained from macroporous electrodes that also offer better performance at high charge/discharge rates than mesoporous electrodes.

■ EXPERIMENTAL SECTION

Materials. Methyl methacrylate (99%), titanium metal (sponge, 3−19 mm, 99.5%), citric acid monohydrate (ACS reagent grade, ≥99.0%), poly(ethylene oxide)−*block*-poly(propylene oxide)−*block*-poly(ethylene oxide) copolymer (molecular weight of 5800, P123), sodium carboxymethyl cellulose (molecular weight of 250 000), lithium ribbon (0.75 mm thickness, 99.9%), and dimethyl carbonate (anhydrous, ≥99.0%) were purchased from Sigma-Aldrich. Phenol (ACS reagent grade), formaldehyde (certified ACS, 37 wt % in water), potassium persulfate (ACS reagent grade), and hydrogen peroxide (certified ACS, 30 wt % in water) were obtained from Fischer Scientific. Hydrochloric acid (ACS reagent grade, 37 wt % in water), ammonium hydroxide (ACS reagent grade, 28−30 wt % in water), and sodium hydroxide pellets (ACS reagent grade) were obtained from Macron Chemicals. Sucrose (ACS reagent grade) was obtained from Mallinckrodt. Ethanol (200 proof, USP grade) was purchased from Decon Laboratories. A suspension of styrene−butadiene rubber (50 wt % in water) was purchased from the MTI Corporation. All of the aforementioned chemicals were not further purified before use. Any deionized water used in these procedures was produced using a Barnstead Sybron purification system (final resistivity > 18 MΩ·cm).

Synthesis of the Ammonium Citratoperoxotitanate(IV) Precursor. This complex was synthesized following a procedure established in the literature,[35] but with a few modifications. To briefly summarize, titanium metal (0.25 g) was combined with 30 wt % aqueous H_2O_2 (20 mL) and concentrated ammonium hydroxide (5 mL). This mixture was stirred on ice for 1 h and then stirred at room temperature until all titanium dissolved. Citric acid monohydrate (1.10 g) was added to the solution. The mixture was heated to 40 °C overnight, and a yellow gel was formed. If needed, further drying was conducted at 70 °C for 3 h.

Synthesis of 3DOM TiO_2/C with Phenol-Formaldehyde Sol as a Carbon Source (PF-TiO_2/C). For this composite and all others, colloidal crystal templates were used. Poly(methyl methacrylate) (PMMA) colloidal spheres were first synthesized using an emulsifier-free emulsion polymerization.[36] Once a suspension of spheres was obtained, a portion of the suspension was placed in a crystallization dish and allowed to sediment. The supernatant was removed via evaporation at ambient temperature. Phenol-formaldehyde (PF) prepolymer sol was also made following a published procedure.[37]

Table 1. Compositions of the Composite Materials

sample	TiO_2 content (wt %)[a]	carbon content (wt %)[b]	organic oxygen content (wt %)[b]	hydrogen content (wt %)[b]	nitrogen content (wt %)[b]
PF-TiO$_2$/C 700 °C	51.5	42.3	2.5	0.9	2.8
sucrose-TiO$_2$/C, 700 °C	46.3	43.0	6.8	0.7	3.2

[a]Determined via thermogravimetric analysis. [b]C, H, and N of the carbonaceous phase determined via combustion analysis, organic oxygen by difference.

The prepolymer was dried using rotary evaporation and redispersed in ethanol to form a 50 wt % ethanolic sol.

The precursor for 3DOM TiO$_2$/C was prepared by first mixing water (1.5 g), ethanol (1.25 g), and concentrated HCl (1.25 g). P123 was then heated at 40 °C until it melted. Liquid P123 (0.8 g) was added to the precursor and stirred until it dissolved. Dried ammonium citratoperoxotitanate(IV) gel (1.6 g) was poured into the precursor, and the mixture was stirred for 15 min. More water (0.25 g) and concentrated HCl (0.25 g) were added to eliminate turbidity, and the precursor was stirred for 5 min. Finally, the precursor was combined with PF sol (0.1 g), and the mixture was stirred overnight.

The colloidal crystal templates were broken into pieces with dimensions of several millimeters and infiltrated with the precursor. For infiltration, the pieces of template were placed at the bottom of a scintillation vial and precursor was pipetted into the vial. To reduce cracking, the liquid precursor was not allowed to cover the top of the templates. Infiltration via capillary action typically took between 2 and 6 h and caused the templates to turn partially translucent once completed. Once infiltration was complete, the templates were wiped clean of excess precursor. Additional solvent was removed by placing the templates in a vacuum oven under low vacuum for 30 min at ambient temperature. Thermal treatment of the templates was performed at 100 °C for 24 h and 140 °C for 24 h. Samples were then heated in a tube furnace under 0.7 L/min of Ar at 1 °C/min to 350 °C and kept at that temperature for 4 h. Depending on the sample, the temperature was then increased at 1 °C/min to either 700, 800, or 900 °C and held at the target temperature for 2 h.

Synthesis of 3DOM TiO$_2$/C with Sucrose as a Carbon Source (Sucrose-TiO$_2$/C). For the sucrose-TiO$_2$/C, a precursor was prepared in fashion similar to the PF-TiO$_2$/C. Initially, water (3.5 g), concentrated HCl (1.25 g), and liquid P123 (0.8 g) were mixed until the P123 dissolved. The ammonium citratoperoxotitanate(IV) gel (1.6 g) was then added to the precursor, and the solution was stirred until it dissolved. If the solution remained slightly turbid, it was heated to 40 °C and was stirred until the turbidity disappeared. Sucrose crystals (0.1 g) were then poured into the precursor, and the solution was stirred overnight. All subsequent processing steps were identical to those performed with the PF-TiO$_2$/C.

Characterization. All samples were analyzed using a variety of analytical techniques. TiO$_2$ content was determined using thermogravimetric analysis (TGA). Samples were loaded in a Netzsch STA 409 PC Luxx thermal analyzer under air flow and heated at 10 °C/min to 1000 °C. C, H, and N analyses were carried out by Atlantic Microlab, Inc. (Norcross, GA) using automatic combustion analysis. Fourier transform infrared red (FTIR) spectra were obtained using a Nicolet Magna-IR 760 spectrometer. Solid samples for FTIR were ground with KBr and pressed into pellets prior to analysis. Raman measurements were carried out using a 514.5 nm Ar$^+$ laser attached to a WiiTech Alpha300R confocal Raman microscope with a DV401 CCD thermoelectric-cooled detector. For a given area, multiple spectra were collected and averaged to provide the final, reported spectrum. To prepare specimens for scanning electron microscopy (SEM), powders of the TiO$_2$/C samples were affixed to double-sided carbon tape placed on an Al stub. These samples were coated with 50 Å of Pt and imaged using a JEOL 6700 instrument operated with an accelerating voltage of 5 kV. Samples for transmission electron microscopy (TEM) were prepared by sonicating powders in ethanol (or dimethyl carbonate) for 5 min, and then dropping the suspension on Cu grids coated with holey carbon. Imaging was performed using a FEI Technai T12 TEM instrument equipped with a LaB$_6$ filament and

operated at 120 kV. Powder X-ray diffraction (PXRD) was conducted using a PANalytical X'Pert Pro diffractometer that was outfitted with a cobalt anode (45 kV, 40 mA) and an X'celerator line detector. Line broadening in the patterns was used to estimate the crystal size via the Scherrer equation. A Rigaku RU-200BVH with a rotating copper anode was used to collect small-angle X-ray scattering (SAXS) patterns. Scattered X-rays were detected using a Siemens Hi-Star multiwire area detector. Nitrogen sorption isotherms at 77 K were obtained using a Quantachrome Autosorb-iQ$_2$-MP analyzer. Prior to analysis, all samples were outgassed for 12 h at 200 °C and 0.001 Torr. The Brunauer−Emmett−Teller (BET) method was applied to obtain surface areas, and pore volumes were calculated using the point P/P_o = 0.995 on the adsorption branch.

Electrochemical Characterization. Before an electrode paste was made, the prepared 3DOM TiO$_2$/C composites were ground and ultrasonicated. Another electrode was made by physically mixing a solution of 50 wt % Degussa P25 TiO$_2$ and 50 wt % MTI Corporation artificial graphite powder. The processed active materials were mixed with Timcal Super P carbon black, aqueous sodium carboxymethyl cellulose (CMC), and aqueous styrene−butadiene rubber (SBR). In the final paste, the weight ratio of components was 84 wt % active material, 10 wt % carbon black, 4 wt % CMC, and 2 wt % SBR. Pastes were coated on either carbon-coated aluminum (kindly provided by Exopack Advanced Coatings) or Cu foil. Electrode films were dried at ambient conditions overnight and then at 24 h at 105 °C. The loading of electrode paste per cm^2 ranged from 1 to 2 mg/cm^2. A punch with a 0.5 in. diameter was used to cut out electrode disks. Half-cells were assembled using CR2032 cells purchased from MTI Corporation. Lithium ribbon served as the counter electrode in the cells and a coated polypropylene separator (Celgard 3501) was utilized to prevent shorts. The electrolyte used in the cells was 1 M LiPF$_6$ dissolved in a 1:1:1 mixture (by mass) of ethylene carbonate, dimethyl carbonate, and diethyl carbonate (purchased from MTI Corporation). All cells were assembled in a glovebox filled with He gas. Cycling was performed on an Arbin Instruments BT2000 from either 1 to 3 V vs Li/Li$^+$ (using carbon-coated Al as a current collector) or from 50 mV to 3 V vs Li/Li$^+$ (using copper as a current collector). Depending on the voltage range used, the C-rate was set so that 1 C = 335 mA per g of TiO$_2$ in the composite (1−3 V) or set at 1 C = 335 mA per g of the composite (0.05−3 V). Specific capacities were calculated in a similar fashion. Cyclic voltammetry (CV) curves were obtained using a Solartron 1287 electrochemical station. Scanning was conducted between 0.05 and 3 V vs Li/Li$^+$ with a scan rate of 5 mV/s and a 1 s integration time.

Impedance spectroscopy was performed on the coin cells using a Solartron 1255B frequency analyzer with an attached 1287 electrochemical interface. The electrode film served as the working electrode and lithium foil served as the counter and reference electrodes. A frequency range of 50 kHz to 500 mHz, an amplitude of 10 mV, and a constant resistance of 100 kΩ were used. The measurements were carried out with cells that were freshly assembled and left to rest for 4 h to facilitate full infiltration with electrolyte, and also on the same cells after they had been galvanostatically cycled 50 times between 3.0 and 0.05 V vs Li/Li$^+$ at 1 C, ending at 3.0 V (fully delithiated). The impedance measurements were performed at the resting potential (between 2.8 and 2.9 V vs Li/Li$^+$). The spectra were fitted to an equivalent circuit (Figure S13c in the Supporting Information) using Wolfram Mathematica 9.0.

RESULTS AND DISCUSSION

Characterization of PF-TiO$_2$/C and Sucrose-TiO$_2$/C. All of the composites were prepared using an ammonium citratoperoxotitanate(IV) gel as a major ingredient. From FTIR and Raman spectroscopy (Figure S1 in the Supporting Information), the gel contains coordinated peroxo and citrate groups bonded in a unidentate fashion. However, there also appear to be free citric acid and Ti centers linked by Ti−O−Ti bonds in the gel. A more detailed analysis is given in the Supporting Information. The chemical composition of PF-TiO$_2$/C and sucrose-TiO$_2$/C pyrolyzed at 700 °C was determined using a combination of thermogravimetry and combustion analysis (Table 1). TGA revealed that the content of TiO$_2$ is slightly greater in PF-TiO$_2$/C than in sucrose-TiO$_2$/C. This difference is most likely due to the fact that twice the mass of sucrose was used in the sucrose-TiO$_2$/C precursor when compared to the mass of PF sol in the PF-TiO$_2$/C precursor. However, pyrolysis of citric acid contributes a substantial fraction of carbon in both the PF-TiO$_2$/C and the sucrose-TiO$_2$/C (10 times the number of moles of citric acid monohydrate is present relative to the PF sol/sucrose). Although the carbon and hydrogen content is similar for both samples, the oxygen content is higher in the carbonaceous fraction of the sucrose-TiO$_2$/C. Elevated oxygen content is expected because sucrose contains an atomic ratio of O to C of nearly one.[38] PF-TiO$_2$/C and sucrose-TiO$_2$/C contain similar amounts of hydrogen and nitrogen. The nitrogen content is significantly elevated in these composites when compared to 3DOM C prepared from the carbonization of resorcinol–formaldehyde resin.[39] Ammonium ions in the gel precursor for the TiO$_2$ appear to be responsible for the increase in nitrogen in the carbonaceous fraction.

To confirm that hard templating was successful, SEM images of the composites were obtained, and representative images are displayed in Figures 1 and S2 (Supporting Information). All
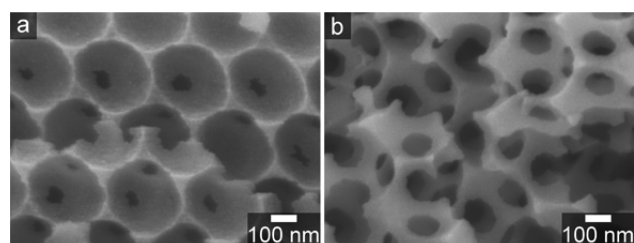

Figure 1. SEM images of (a) PF-TiO$_2$/C and (b) sucrose-TiO$_2$/C composites pyrolyzed at 900 °C. Images corresponding to other pyrolysis temperatures are shown in Figure S2 in the Supporting Information.

materials contain an interconnected, face-centered-cubic array of macropores that facilitates penetration of electrolyte throughout these materials. Some disorder (micrometer-scale voids, broken struts) is present in the network. Although the 3DOM structure is similar for both PF-TiO$_2$/C and sucrose-TiO$_2$/C, a few differences can be observed. For the PF-TiO$_2$/C, many regions have interconnecting windows with a narrow diameter. This is typical of surface-templated 3DOM materials synthesized with precursors that have more favorable interactions with the hard template. The ethanol in the PF-TiO$_2$/C can wet the PMMA colloidal crystal better than the purely water-based precursor for sucrose-TiO$_2$/C, explaining the occurrence of surface templating. A more "skeletal" volume-

templated structure with larger windows between adjacent macropores is present in the sucrose-TiO$_2$/C that likely arises from repulsive interactions between the highly polar precursor and the nonpolar template.[25]

Transmission electron microscopy provides a more complete understanding of the morphology, including the location/size of TiO$_2$ crystallites and mesopores. From examination of Figure 2, TiO$_2$ crystallites are so small that they cannot be observed at
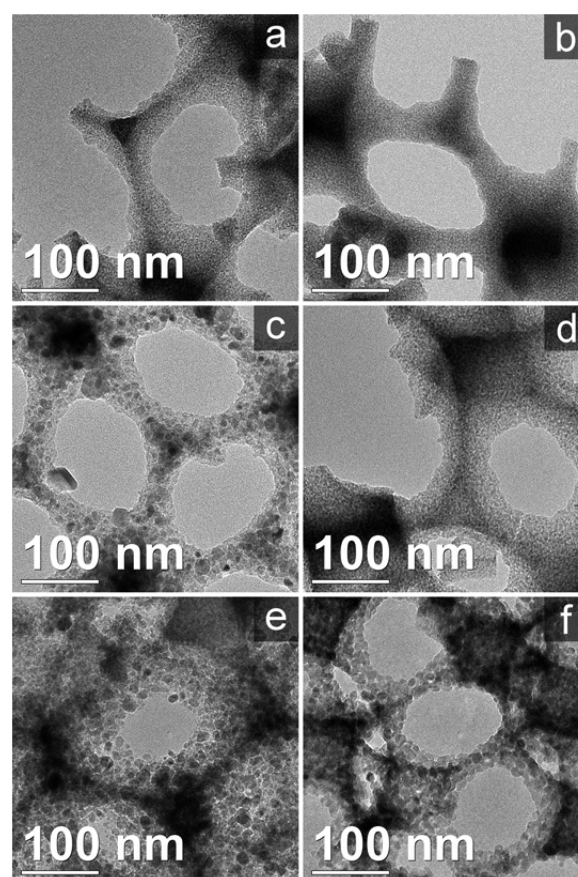

Figure 2. TEM micrographs of PF-TiO$_2$/C and sucrose-TiO$_2$/C pyrolyzed at various temperatures. The first column shows PF-TiO$_2$/C pyrolyzed at (a) 700 °C, (c) 800 °C, and (e) 900 °C. The second column shows sucrose-TiO$_2$/C pyrolyzed at (b) 700 °C, (d) 800 °C, and (f) 900 °C.

moderate magnifications for composites pyrolyzed at 700 °C. The carbon matrix provides a barrier for the sintering of TiO$_2$ crystallites, resulting in their small size. Small, bright lines also snake across the composites at those temperatures, and result from disordered mesopores templated from P123. Higher magnification images (Figure S3 in the Supporting Information) reveal the crystallites via diffraction contrast. These crystals are smaller than 5 nm in both PF-TiO$_2$/C and sucrose-TiO$_2$/C. This is smaller than TiO$_2$ crystals in 3DOM TiO$_2$/C synthesized using trifluoroacetic acid or 2,4-pentanedione as chelating agents at the same pyrolysis temperature.[17] Because carbon content is higher in the PF-TiO$_2$/C and sucrose-TiO$_2$/C than the 3DOM TiO$_2$/C synthesized in the aforementioned paper, sintering of TiO$_2$ is suppressed even further. Decomposition of the citric acid may also assist in inhibiting the sintering of TiO$_2$. Carboxylate groups of the citric acid are bonded to Ti ions (see the Supporting Information), and the citric acid can carbonize into shells that surround growing TiO$_2$

nuclei during pyrolysis. After pyrolysis at 800 and 900 °C, a distinct increase in the crystal size occurs, indicating that the temperature is sufficiently high to allow for extensive sintering. At 800 °C, PF-TiO$_2$/C experiences more pronounced sintering than sucrose-TiO$_2$/C, albeit in localized areas. For the PF-TiO$_2$/C sample pyrolyzed at 900 °C, many crystallites of TiO$_2$ are localized on the surface of the composite. In the case of the sucrose-TiO$_2$/C, areas that suffer from extensive sintering contain crystallites conforming to the structure of the 3DOM network.

TEM imaging also reveals inhomogeneities in the location and size of TiO$_2$ crystallites in the composites (Figure 3). At
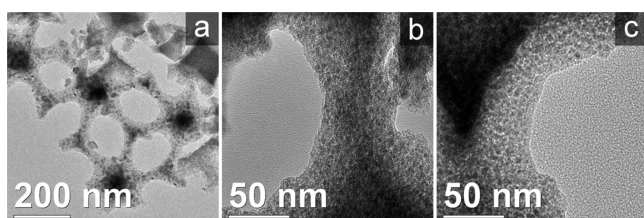

Figure 3. TEM micrographs highlighting inhomogeneities in the location/size of TiO$_2$ crystallites in the composites. (a) Regions with large and small crystallites of TiO$_2$, coexist for the PF-TiO$_2$/C sample pyrolyzed at 800 °C. For the images of (b) PF-TiO$_2$/C and (c) sucrose-TiO$_2$/C pyrolyzed at 900 °C, crystallites of TiO$_2$ (or titanium oxycarbide) are much smaller than those imaged in Figure 2

higher pyrolysis temperatures (800 and 900 °C), there is a substantial nonuniformity in the size of the observed crystallites. Many regions contain crystals that are much smaller than those found adjacent regions (compare Figure 3a–c with the counterparts in Figure 2). This variation is highlighted especially well by comparing the top right of Figure 3a with the bottom center of the image. Areas with a high concentration of TiO$_2$ facilitate sintering and lead to larger crystallites. As shown later, titanium oxycarbide is also present in these composites. Regions with smaller crystallites contain a high concentration of the oxycarbide phase. Selected area electron diffraction (SAED) of these areas (specifically those shown in Figure 3b,c), reveal diffraction rings that cannot be indexed to anatase or rutile TiO$_2$ but match a titanium oxycarbide phase also found in the PXRD patterns discussed below (see Figure S4 in the Supporting Information).

By examining the PXRD patterns of the composites (Figures 4 and S5, Supporting Information), one can observe that similar series of phase transformations occur for both PF-TiO$_2$/C and sucrose-TiO$_2$/C. For composites pyrolyzed at 700 °C, strong peaks corresponding to anatase or rutile TiO$_2$ are absent. A broad peak near 29.4° 2θ matches the (101) reflection of anatase TiO$_2$ and is overlaid on a shoulder spanning from 22.5 to ~40° 2θ from amorphous carbon.[38] Another peak near 51° 2θ is attributed to the carbon framework produced from the various carbon-containing precursors (denoted with a cross in Figure 4).[38,40] Once the pyrolysis temperature is increased to 800 °C, anatase and rutile reflections appear in the patterns. Rutile is the major TiO$_2$ polymorph at 900 °C. This is expected because rutile is the thermodynamically stable phase for bulk TiO$_2$ and forms at high temperatures.[41] Several other peaks are observed in the patterns of materials pyrolyzed at 800 and 900 °C. Because these reflections are positioned between cubic TiC and TiO and follow the pattern of a face-centered cubic structure, they are assigned to a titanium oxycarbide (TiO$_x$C$_y$)
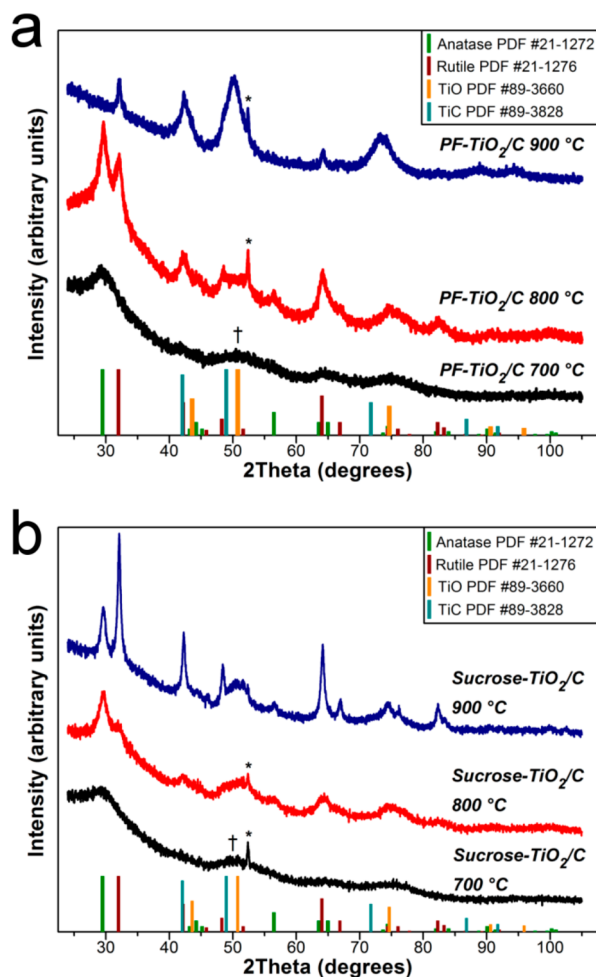

Figure 4. PXRD patterns for (a) PF-TiO$_2$/C and (b) sucrose-TiO$_2$/C pyrolyzed at different temperatures. The cross marks the location of a peak from the carbon network and the asterisk marks a reflection from the Al sample holder.

phase.[42] All the d-spacings of the reflections shown in the PXRD patterns (see Figure S5 in the Supporting Information) closely match those of the SAED patterns shown in Figure S4 in the Supporting Information. This provides further confirmation that titanium oxycarbide is present in certain areas of the 3DOM composites. The titanium oxycarbide is formed from the carbothermic reduction of TiO$_2$,[13,20] and this process occurs at unusually low temperatures for PF-TiO$_2$/C and sucrose-TiO$_2$/C.[43] Small crystallite sizes and the abundance of carbon facilitate the carbothermic reduction.[20,43,44] Indeed, this process occurs so quickly that the intermediate Magnelí phases that typically form during the reduction[42] are not even identified in the PXRD patterns.

Crystallite sizes of anatase TiO$_2$, rutile TiO$_2$, and titanium oxycarbide were estimated using the line width of sufficiently intense reflections in the PRXD patterns and are presented in Table 2. At 700 °C, the reflections are so weak that they cannot be satisfactorily fit. Again, this is due to a suppression of sintering by the intervening carbon matrix. Once the pyrolysis temperature is increased to 800 °C, TiO$_2$ crystallite sizes can be determined. PF-TiO$_2$/C contains larger anatase TiO$_2$ crystallites than those in sucrose-TiO$_2$/C. This difference may be from the increased proportion of the secondary carbon phase in sucrose-TiO$_2$/C. Even though confinement of TiO$_2$ by the

Table 2. Structural and Textural Parameters of PF-TiO$_2$/C and Sucrose-TiO$_2$/C

sample	anatase crystallite size (nm)	rutile crystallite size (nm)	titanium oxycarbide crystallite size (nm)	BET surface area (m^2/g)	pore volume (mL/g)
PF-TiO$_2$/C, 700 °C	a	a	c	226	0.44
PF-TiO$_2$/C, 800 °C	8.3	8.5	b	375	0.40
PF-TiO$_2$/C, 900 °C	c	10.3	3.2	412	0.60
sucrose-TiO$_2$/C, 700 °C	a	a	c	225	0.43
sucrose-TiO$_2$/C, 800 °C	6.7	8.8	b	281	0.47
sucrose-TiO$_2$/C, 900 °C	10.0	16.3	3.9	326	0.65

[a]Reflections too weak to be analyzed via the Scherrer equation. [b]Phase present, but too weak to be analyzed via the Scherrer equation. [c]Phase not detected in PXRD pattern.

carbonaceous fraction occurs in PF- and sucrose-TiO$_2$/C, the size of TiO$_2$ crystallites exceeds 10 nm in all samples once pyrolysis is conducted 900 °C. Rutile TiO$_2$ grows more rapidly than anatase TiO$_2$,[45] and this is borne out by the larger rutile crystal size in sucrose-TiO$_2$/C. Interestingly, larger rutile crystallites are found in sucrose-TiO$_2$/C than in PF-TiO$_2$/C, but this may be from the increased conversion of TiO$_2$ to titanium oxycarbide in PF-TiO$_2$/C. A decreased content of TiO$_2$ in PF-TiO$_2$/C due to the conversion may limit sintering. Reflections from the titanium oxycarbide phase can be fitted for materials pyrolyzed at 900 °C. The average size of oxycarbide crystallites is 3.2 nm in PF-TiO$_2$/C and 3.9 nm in sucrose-TiO$_2$/C, and these sizes are similar to TiC formed via carbothermic reduction in mesoporous TiO$_2$/C materials.[13,20] Titanium oxycarbide experiences slower sintering and grain growth kinetics than either TiO$_2$ polymorph.

Because inhomogeneities were detected using TEM, confocal Raman microscopy was also used to investigate the spatial variations in the TiO$_2$ polymorph. Spectra of PF-TiO$_2$/C and sucrose-TiO$_2$/C pyrolyzed at different temperatures are presented in Figure 5. Depending on the area of sample analyzed, Raman modes corresponding to the anatase or rutile polymorph are found.[46,47] Rutile TiO$_2$ is detected in the PXRD patterns for composites pyrolyzed at 800 and 900 °C, so the appearance of rutile Raman modes are expected. However, the appearance of peaks that match the position of rutile TiO$_2$ modes is unexpected for samples pyrolyzed at 700 °C. It appears that rutile TiO$_2$ nucleates from ammonium citratoperoxotitanate(IV) or undergoes a phase transition (from either amorphous TiO$_2$ or anatase TiO$_2$) to rutile at very small crystallite sizes (below 5 nm). At that size, rutile is thermodynamically unstable relative to anatase when no surrounding carbon matrix is present.[45] When TEM images for sucrose-TiO$_2$/C pyrolyzed at 700 °C (Figure S3b in the Supporting Information) are examined, the spacing between lattice fringes of TiO$_2$ crystals is ~0.32 nm. This distance corresponds to the d-spacing for the (110) plane of rutile TiO$_2$. Anatase is found in other areas with a lattice spacing of ~0.35 nm (corresponding to the (101) plane), and this is shown for PF-TiO$_2$/C pyrolyzed at 700 °C (Figure S3a in the Supporting Information). Another contribution to the vibrational modes that match rutile TiO$_2$ may be from titanium oxycarbide crystallites. While crystals of stoichiometric cubic TiC (and TiO) lack Raman-active modes, crystals with cationic vacancies display Raman modes at positions nearly identical to those of rutile TiO$_2$.[48,49] It is possible that conversion from TiO$_2$ to the oxycarbide would produce crystallites with defects.[49]

Confocal Raman microscopy was also used to analyze the carbonaceous components in these composites. The corresponding spectra are presented in Figure S6 in the Supporting

Information. Two characteristic bands are observed, both of which result from vibrations in the six-membered carbon rings that are present in the amorphous carbon. Centered at ~1600 cm^{-1} is the G band, which arises from stretching of bonds between sp^2-hybridized carbon atoms.[50] At ~1350 cm^{-1} is the D band, which results from a breathing mode in any sp^3-hybridized carbon atoms present in the ring.[50] Not surprisingly, the intensity of the G band relative to the D band increases as the pyrolysis temperature is raised for both PF-TiO$_2$/C and sucrose-TiO$_2$/C (see Table S1 in the Supporting Information). This indicates that the fraction of sp^3-hybridized carbon atoms decreases at high pyrolysis temperatures, since higher temperatures allow for the removal of heteroatoms and the formation of extended aromatic (graphitic) domains.

The pore texture of the composite materials was analyzed by SAXS and by N$_2$ gas sorption to estimate the surface area of the various samples, determine pore volumes, and probe changes in meso-/microporosity. All of the N$_2$ sorption isotherms presented in Figure S7 in the Supporting Information reveal sharp rises in the volume of gas adsorbed at low (P/P_o < 0.001) and high (P/P_o > 0.9) relative pressures. Micropores present in the amorphous carbon are responsible for the rise at the low pressure range, and the templated macropores are responsible for the rise at high pressures. Although the P123 surfactant was present in the precursor, little hysteresis is present in the isotherms. For PF-TiO$_2$/C, very narrow hysteresis loops are present in all samples. In contrast, sucrose-TiO$_2$/C only has a narrow hysteresis loop when pyrolyzed at 700 °C. However, TEM images show changes in contrast expected for disordered mesopores or perhaps isolated micelles (see Figures 2 and 3). It appears that either the concentration of surfactant was too low for the formation of any ordered mesostructure, or that the interactions between the surfactant and the other components of the precursor are insufficient or unfavorable for self-assembly. SAXS patterns of the composites suggest that a well-defined mesostructure is absent. These patterns are either free of scattering peaks or contain a very weak scattering peak near 1.5° 2θ (Figure S8 in the Supporting Information). Even without substantial mesoporosity, all composites have BET specific surface areas greater than 200 m^2/g and high pore volumes (see Table 2). As the pyrolysis temperature is brought higher, both the specific surface area and pore volume the composites increase. This increase is mainly from the continued formation of micropores in the amorphous carbon component (see Figure S9 in the Supporting Information); this phenomenon is also observed in other nanostructured TiO$_2$/C composites.[17,20]

At this point, it is important to consider the location and polymorph of the TiO$_2$ crystallites in the composites in more detail. Based on results obtained from SEM and TEM images,
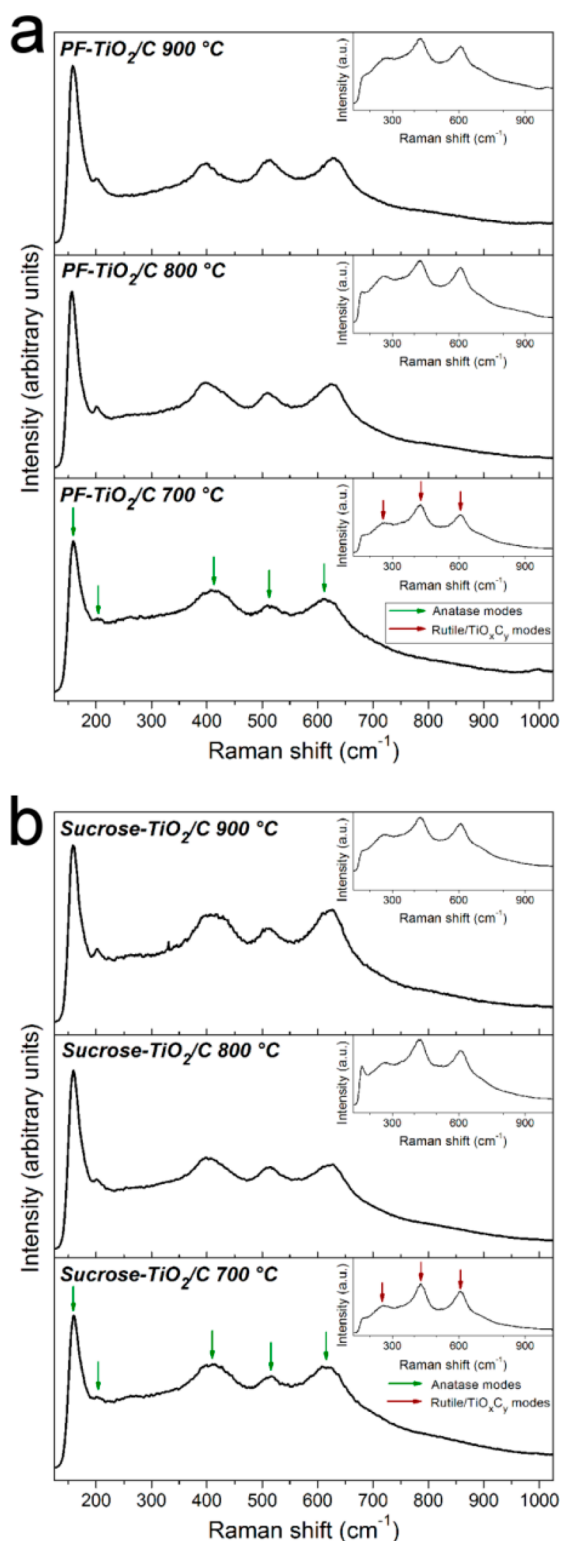
Figure 5. Raman spectra for (a) PF-TiO$_2$/C and (b) sucrose-TiO$_2$/C in the spectral region that reveals TiO$_2$ lattice vibrations. Regions are found in all the samples that contain anatase and/or rutile modes (see insets). It is possible that vibrations from a defective TiO$_x$C$_y$ phase overlap with rutile TiO$_2$ vibrations.

TiO$_2$ crystallites are distributed throughout the carbon matrix in the walls and nodes of the 3DOM network. From studies of the citratoperoxotitanate(IV) complex, it has been determined that the complex is hydrophilic and carries a negative charge.[35]

Even if that complex is different in the gel, functional groups on the citric acid ligands and the peroxo ligands themselves should be able to interact (via intermolecular bonding) with the water and other hydrophilic components in the precursor. Similar behavior was reported by Petkovich et al. for 3DOM TiO$_2$/C prepared using 2,4-pentanedione as a chelating agent.[17] In both the earlier report and here, the complex interacts with other components in the precursor and a fairly homogeneous distribution of TiO$_2$ is observed. Inhomogeneities may arise for PF-TiO$_2$/C and sucrose-TiO$_2$/C if the Ti cations are bound extensively to carboxylate groups present on the citric acid and the peroxo ligands. In this case, the complexes are less likely to bond to hydroxyl functionalities present in the PF sol/sucrose, hindering the interaction of the various components. An alternate possibility is that excess ammonium citrate, which is not bonded to Ti cations, phase demixes from the other components of the precursor, and generates extensive carbon-rich domains. It is more likely this occurs, given that free carboxylate moieties are present in the gel precursor and only unidentate carboxylate binding is detected in the ammonium citratoperoxotitanate(IV) gel precursor (see Figure S1 and discussion in the Supporting Information). Rapid conversion of small TiO$_2$ grains to titanium oxycarbide (perhaps in carbon-rich areas) could also contribute to heterogeneities. Once TiO$_2$ is converted to titanium oxycarbide, the oxycarbide grains grow slowly, unlike the unconverted TiO$_2$. Slight differences in crystallite location between the PF- and sucrose-TiO$_2$/C precursor systems may arise from the ethanol in the PF system. A less favorable interaction between the ionic precursor and the ethanol may result in more separation from the precursor, leading to more clustering of TiO$_2$ crystals near the surface, as is observed in PF-TiO$_2$/C electron microscopy images (Figure 2).

Another curious aspect of this system is that small rutile TiO$_2$ nuclei are present in the carbon matrix. The transformation from anatase to rutile does not generally occur until anatase crystals reach ~11 nm in size.[41] Dopants can alter the point at which the phase transition occurs, but the two likely dopants here, carbon and nitrogen, are known to suppress that transformation.[45] Additionally, the carbon matrix should limit crystal growth and reduce the number of interfaces between anatase crystallites that can serve as nucleation sites for rutile.[51] The preferential nucleation of rutile at low temperatures has been observed in hydrothermal syntheses that use a titanium source and citric acid.[52] Researchers postulate that the octahedral complexes of titanium and citric acid undergo condensation to form linked edge-sharing units. Due to the structural similarity of this arrangement to the TiO$_6$ clusters in rutile, the rutile phase preferentially forms.[52] This could also occur in the composites studied herein. Another factor may be that reducing gases produced from pyrolysis of the citric acid and PF sol/sucrose generate oxygen vacancies in the TiO$_2$. Oxygen vacancies are known to assist in the transformation of anatase to rutile.[45,53] While these two explanations address the presence of rutile, they do not explain the coexistence of anatase TiO$_2$. It could be that some of the citratoperoxotitanate(IV) complexes condense at an earlier processing stage (as observed from Ti−O−Ti linkages described in the Supporting Information) and form face-sharing octahedra. This is similar to the situation for TiO$_6$ clusters in anatase, leading to its preferential nucleation.[52]

Electrochemical Characterization. For electrochemical testing, PF-TiO$_2$/C and sucrose-TiO$_2$/C samples pyrolyzed at

700 and 800 °C were cycled in two different voltage windows. Due to increases in TiO_2 crystal size and widespread formation of titanium oxycarbide, samples pyrolyzed at 900 °C were not tested. This section first presents electrochemical cycling data in the window between 1 and 3 V vs Li/Li^+, which should be dominated by insertion/extraction reactions in TiO_2. However, less than 50 wt % of any given electrode is TiO_2. Full utilization of the active material (TiO_2 and carbon) is explored by changing the voltage window to between 0.05 and 3 V vs Li/Li^+, allowing for lithium insertion/extraction into amorphous carbon. Substantial improvements in the capacity of the composites are realized by using the wider window. A comparison is also made to 3DOM C synthesized using PF sol, and this material is described in the Supporting Information (see Figures S10 and S11, and associated text in the Supporting Information).

When cycling is limited to the window between 1 and 3 V vs Li/Li^+, the impact of increased pyrolysis temperature and amorphous carbon content are observed. Figure 6a shows the capacities at different cycling rates, and Figure 7 shows extended cycling at a rate of C/2. Raising the pyrolysis temperature has a similar effect for both PF-TiO_2/C and sucrose-TiO_2/C; capacities decrease at 800 °C for all cycling

Figure 6. Capacities at different C-rates for PF-TiO_2/C and sucrose-TiO_2/C pyrolyzed at 700 and 800 °C. In panel a, the voltage window extends between 1 and 3 V vs Li/Li^+ for the tests, and the specific capacities/currents are per gram of TiO_2 in the electrode. In panel b, the voltage window used for these tests extends from 0.05 to 3 V vs Li/Li^+ and the specific currents/capacities are per mass of composite in the electrode. A 3DOM C reference material pyrolyzed at 700 °C is also shown in panel b, and cycled with the same conditions as the composites.

rates when compared to electrode materials pyrolyzed at 700 °C. This is borne out in both the rate performance and the extended cycling data. Extensive crystallite growth occurs when pyrolysis temperatures are increased from 700 to 800 °C; moreover, the titanium oxycarbide forms when PF-TiO_2/C and sucrose-TiO_2/C are pyrolyzed at 800 °C. These processes counteract any benefit derived from the enhancement of the electronic conductivity of the carbon framework generated by higher pyrolysis temperatures.[54] The benefits of improved electronic conduction in the carbon framework are negated in another fashion. While the amorphous carbon in the composites restricts crystal growth, it also blocks lithium-ion transport to the active TiO_2 crystallites. An ideal composite of carbon and active material should contain either a minimal conformal coating of carbon[55] or (for an active material with slow ion conduction) as few contact points with carbon as possible.[56] Electronic conductivity is then facilitated without hindering ionic transport. Unfortunately, PF-TiO_2/C and sucrose-TiO_2/C contain abundant carbon that blocks ion transport to TiO_2 crystallites in the 3DOM network. As a consequence, capacities deteriorate at high charge/discharge rates. However, the capacities for insertion/extraction of Li^+ at low rates are quite good, and exceed 0.5 Li^+ per unit of TiO_2. Interestingly, the capacities of the TiO_2/C anodes increase during repeated charging and discharging at a C/2 rate and only begin to level out after roughly 80 charge/discharge cycles. This capacity rise has been observed for other TiO_2-containing anodes,[19,57−59] and is typical of lithium storage in a polymeric gel layer that can form on carbon and metal oxide anode materials.[60−62] During electrochemical cycling, the gel dissolves into the carbonate solvent during discharge and re-forms during charging.[60] Further evidence of gel layer formation and dissolution (via analysis of cyclic voltammograms) is discussed in the Supporting Information.

Changing the precursor to the less toxic one used for sucrose-TiO_2/C induces minor changes in the observed capacities when compared to PF-TiO_2/C. Capacities are generally higher for PF-TiO_2/C than for sucrose-TiO_2/C after these composites are pyrolyzed at 700 °C. This reverses when pyrolysis is conducted at 800 °C. Sucrose-TiO_2/C has higher capacities than its counterpart until 2C (at which point they are about equal). Similar to what is discussed above, these differences in capacity stem from variations in carbon content and TiO_2 crystallite size. At 700 °C, both types of composite have extremely small crystallites, but the composite with PF-TiO_2/C contains more TiO_2 than the sucrose-TiO_2/C. Extra carbon can impede Li^+ transport through sucrose-TiO_2/C, causing the decreased capacity at high rates. Greater oxygen content in the carbonaceous phase of the sucrose-TiO_2/C might also result in lower electronic conductivity and lower capacities. For composites pyrolyzed at 800 °C, the material with smaller anatase crystallites (sucrose-TiO_2/C) has higher capacities at high rates. It should be noted that the maximum difference in capacities is about 30% for materials pyrolyzed at 700 °C and about 20% for 800 °C (see Figure 6). From the standpoint of the lithium-ion insertion/extraction, there are no drawbacks to using the safer precursor for 3DOM TiO_2/C.

Possible mechanisms for insertion/extraction into the composite electrode can be explored for the composites via analysis of their voltage profiles (Figure 8). Easy resolution of a biphasic intercalation mechanism versus solid solution or interfacial charge storage is possible. For instance, the voltage profiles show a sloping profile without a noticeable plateau
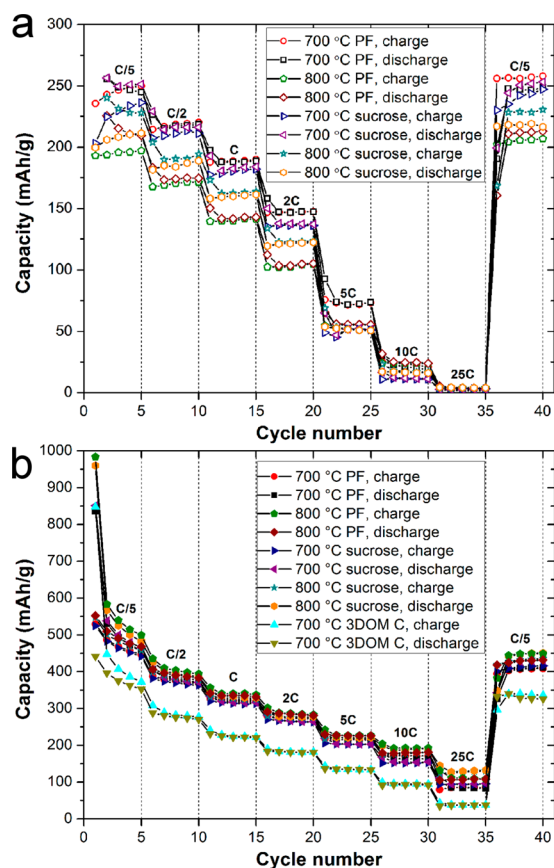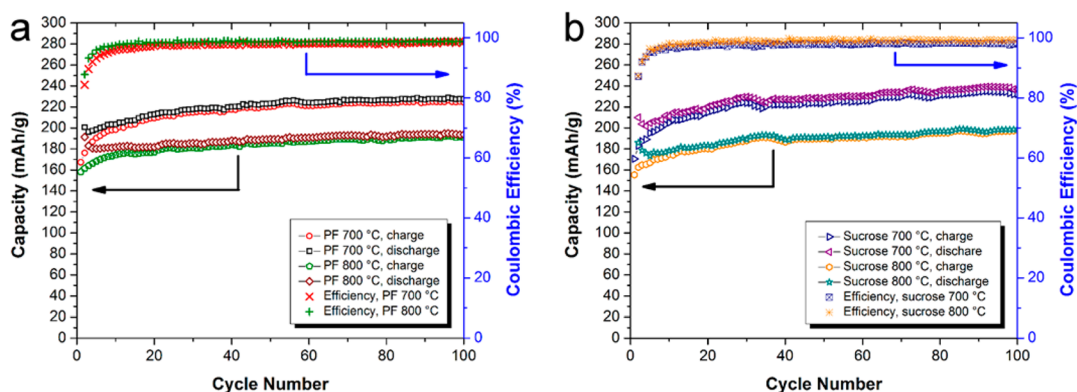
Figure 7. Extended cycling (100 cycles) conducted at a rate of C/2 for (a) PF-TiO$_2$/C and (b) sucrose-TiO$_2$/C. Coulombic efficiencies are shown for all of the materials. The voltage window extends between 1 and 3 V vs Li/Li$^+$ for the tests.
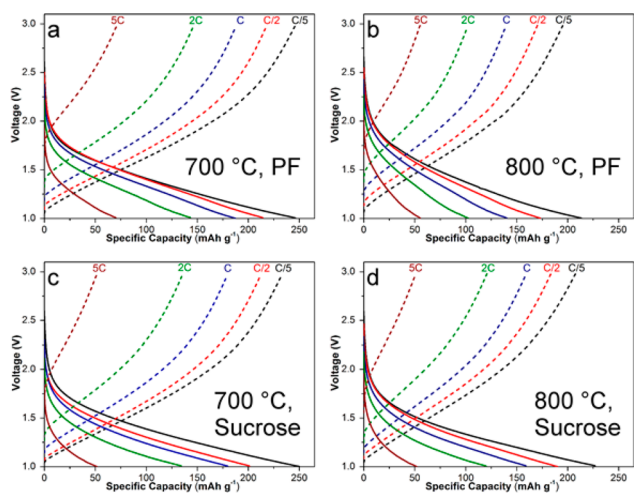

Figure 8. Voltage profiles for charging and discharging at various rates (using a window from 1 to 3 V vs Li/Li$^+$). Graphs for the PF-TiO$_2$/C composites for pyrolysis at (a) 700 °C and (b) 800 °C are shown at the top, and graphs for the sucrose-TiO$_2$/C composites for pyrolysis at (c) 700 °C and (d) 800 °C are shown at the bottom. Sloping profiles are observed for all of the composites tested.

(Figure 8). The plateau for two-phase intercalation in anatase should occur at ∼1.7 V at low C rates,[8] but it is absent in Figure 8a−d. Because the anatase crystallites are so small, the emergence of two phases (and an associated phase boundary) is postulated to be energetically unfavorable, leading to Li$^+$ solid solution insertion/extraction.[63] A sloping profile occurs in this solid solution case. Another contribution can be attributed to intercalation into rutile TiO$_2$, which also displays a sloped voltage at small crystallite sizes.[64] Either intercalation into a rutile-like lithiated form of TiO$_2$ with an extended solid solution range may contribute to this behavior,[65] or a phase change may have occurred early on in cycling.[64,66] Once an irreversible phase change from rutile TiO$_2$ to a lithiated hexagonal titanate takes place, insertion and extraction of Li$^+$ only occurs in the hexagonal phase via a solid solution mechanism.[66] Carbon should contribute only a limited amount to the capacity because only certain sites in the amorphous matrix can undergo insertion/extraction in this range.[38,67] Li$^+$ storage/extraction into the polymeric gel layer may also contribute, albeit to a limited extent, to the sloping profiles.

Because amorphous carbon comprises a substantial fraction of these composites, better utilization of the entire mass of the

electrode is possible by cycling the electrodes down to 0.05 V vs Li/Li$^+$ (Figure 9). A large percentage (over 50% for all rates)
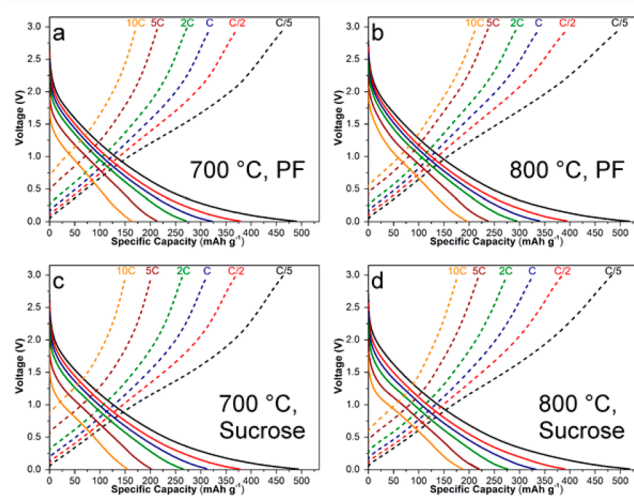

Figure 9. Voltage profiles for charging and discharging in an extended voltage window from 3 V vs Li/Li$^+$ to 0.05 V vs Li/Li$^+$. Graphs for the PF-TiO$_2$/C composites for pyrolysis at (a) 700 °C and (b) 800 °C are shown at the top, and graphs for the sucrose-TiO$_2$/C composites for pyrolysis at (c) 700 °C and (d) 800 °C are shown at the bottom. Specific capacities and currents are per mass of all active material (carbon and TiO$_2$) in the composite.

of the capacity comes from the region below 1 V vs Li/Li$^+$, which includes Li$^+$ insertion/extraction events into amorphous carbon. Staging behavior typical of graphitic carbon is not present,[67] instead the voltage profile is sloped. Amorphous carbon, with its abundance of different intercalation environments, displays a sloping voltage profile like what is observed in Figure 9.[67] Similarly, part of the capacity in Figure 9 comes from TiO$_2$, especially in the range of 1 to 3 V vs Li/Li$^+$. Figure S12 in the Supporting Information provides cyclic voltammograms that show further evidence of the contribution of TiO$_2$ in that range, and potentially at lower voltages. An extended discussion of the voltammograms and a comparison to the 3DOM C reference material is also given in the Supporting Information. Changing to a larger voltage window may also overcome any kinetic barriers (e.g., an overpotential) to intercalation into highly confined TiO$_2$ crystallites, allowing for better utilization of the active material. Even in nano-

particulate TiO_2, higher capacities are obtained by extenting the voltage window.[68]

A clearer picture of the changes induced by cycling in a wider voltage window can be obtained by examining rate performance data vs cycle number and the morphology of the cycled electrodes. Capacities for the electrodes cycled between 0.05 and 3 V vs Li/Li+ are considerably higher than those for electrodes cycled in a narrow voltage window (Figure 6b). This boost in overall capacity is especially noticeable at high rates, with the PF-TiO_2/C and sucrose-TiO_2/C electrodes retaining roughly 150 to 200 mAh/g of capacity at 10C. Because the specific currents/capacities are per 84 wt % of the active mass of the electrode, the overall improvement in capacity is even greater than what is shown in Figure 6b when compared to those electrodes cycled in the narrower window. Similar to data obtained from the electrodes cycled in a narrow voltage window, slight increases in the charge and discharge capacity occur when returning to a C/5 rate for the electrodes cycled in the wider window. Again, it is probably the contribution of a polymeric gel that contributes to the increase. In contrast to electrodes cycled between 1 and 3 V vs Li/Li+, capacities for all the PF-TiO_2/C and sucrose-TiO_2/C electrodes are similar when they are cycled in the wide window. Increasing the pyrolysis temperature results in a slight improvement in capacities at high rates (25 C), perhaps due to better electronic conductivity in the amorphous carbon.

Another key difference between cycling in the two ranges is that decomposition of the electrolyte should occur in the lower voltage range, leading to formation of a stable SEI layer.[7] Formation of this layer is responsible for the large drop in the initial cycling capacity (see cycles 1 and 2 in Figure 6b), as electrolyte degradation takes place. When TEM micrographs of electrodes (washed in dimethyl carbonate to preserve the SEI) taken after cycling are compared, a conformal SEI layer is found on the surface of the electrode materials cycled in the wide voltage window (Figure S14 in the Supporting Information). In contrast, the SEI layer is absent (or extremely thin) in the electrodes cycled between 1 and 3 V vs Li/Li+ (see Figure S14c in the Supporting Information for an example). The SEI layer is composed of light elements (Li, C, O and F), which explains why little contrast is observed between this layer and the composite.[7] Despite the poor contrast, it is still clear that the SEI layer does not block the macropore windows, preserving the interconnected pore structure.

Finally, a 3DOM carbon reference material without any TiO_2 (see the Supporting Information) was cycled in the voltage window from 0.05 to 3 V vs Li/Li+. When compared to PF-TiO_2/C and sucrose-TiO_2/C in Figure 6b, 3DOM C has lower capacities than the composites at all rates. The difference in capacities is especially pronounced at moderate charge/discharge rates; the capacity of the composites outstrips that of the 3DOM C by ~100 mAh/g. This is akin to what has been observed for mesoporous TiO_2/C composites when compared to mesoporous C.[16,18] Additionally, the PF-TiO_2/C and sucrose-TiO_2/C composites have comparable[18,23] or greater capacities[16,22] at high charge/discharge rates when compared to mesoporous TiO_2/C composites pyrolyzed at higher temperatures. Returning to the reference material used in this study, the contribution to the charge/discharge capacity in the range from 1 to 3 V vs Li/Li+ is lower for 3DOM C than for the composites. This is indicated by the steep slope of the voltage profile (see Figure S15 in the Supporting Information) in this range. Again, this is a telling sign that the TiO_2 contributes to

the overall capacity, especially at high rates. A substantial advantage is then achieved by the use of TiO_2 for the anode material. For rates greater than 1 C, PF-TiO_2/C and sucrose-TiO_2/C deliver greater capacities than 3DOM carbon with mesoporous walls,[69] and lignin-derived carbon.[70] Even compared to highly conductive nanocarbon materials, i.e., carbon nanotube/mesoporous carbon composites[71] and graphene/carbon nanofiber composites,[72] the TiO_2/C composites provide similar capacities at high rates (10 C).

Besides providing control over the relative placement of the titania in a carbon composite electrode,[17] the colloidal crystal templating method produces 3DOM composite structures with improved charge transport properties compared to physical mixtures of TiO_2 nanoparticles and conductive carbon. This was demonstrated through electrochemical impedance spectroscopy, comparing as-made and cycled electrodes of the materials discussed above with electrodes prepared using a mixture of P25 TiO_2 and graphite (Figure S13 and Table S2, Supporting Information). In all cells, the resistances increased during the first 50 cycles due to the formation of an SEI layer. Comparisons are therefore made for cells after 50 cycles. The series resistance R_1 (see Figure S13c, Supporting Information) was lower for all 3DOM materials compared to the P25/graphite composites, even though graphite is more conductive than PF- or sucrose-derived carbon. The lower resistance is interpreted to be the result of better contact between active material components in the more continuous 3DOM structure that contains TiO_2 nanoparticles intimately embedded in the carbon phase. The resistance R_2, which is related to ion transport across a surface,[17] is also lower for PF-TiO_2/C and sucrose-TiO_2/C materials than for P25/graphite (except for sucrose-TiO_2/C 700 °C), likely due to the more accessible surface of the 3DOM structure. This is not the case for resistance R_3 associated with surfaces that are less accessible to the electrolyte, because access to the TiO_2 nanoparticles is partially blocked by the surrounding carbon phase. On the other hand, R_3, part of a modified Randles cell, is significantly lower for all 3DOM composite materials that contain smaller TiO_2 crystallites and carbon components than P25/graphite composites and provide easier insertion of Li+ into active material. Warburg coefficients (σ) are significantly smaller for all 3DOM materials than for P25/graphite, also indicating improved Li+-ion diffusion in the former. Overall, the lowest resistances are found in the PF-TiO_2/C materials that exhibited the highest capacities at high rates.

A question still remains: why is the capacity of the composites greater than that of the 3DOM carbon anode? Several explanations have been put forward for capacity boost observed with mesoporous TiO_2/C in the literature, including that the high surface area of the composites facilitates insertion/extraction reactions.[16,18,22] Interestingly, the surface areas for the 3DOM TiO_2/C composites presented in this chapter are lower than what is attained in mesoporous TiO_2/C,[18] yet the 3DOM materials have equivalent or greater capacities at high rates. We posit two possibilities for the increase in capacities when the 3DOM TiO_2/C is cycled in an extended voltage window. First, a synergistic improvement in capacity in TiO_2/C nanocomposites may arise from the numerous interfaces that exist in these materials. Diffusion of lithium is easier through grain boundary defects, and possible storage of lithium can take place at the interfaces (much like the situation with amorphous carbon).[73] Second, extending the window may simply provide a driving force for greater utilization of the TiO_2 phase, as has

been observed by Pfanzelt et al. for rutile TiO$_2$.[68] Future studies that determine lithium-ion diffusion rates in the composites, determine at what voltages specific insertion events occur, and determine the bonding environment around inserted lithium ions may assist in resolving this open question.

CONCLUSION

In this paper, a set of 3DOM TiO$_2$/C anodes, synthesized using reduced toxicity precursors, were shown to exhibit high capacities when cycled in different voltage windows. Both the pyrolysis temperature used during processing and, to a lesser extent, the carbon source in the precursor influence the final structure of the composite. While the PF- and sucrose-TiO$_2$/C retain a 3DOM structure dictated by the colloidal crystal template, irrespective of pyrolysis temperature, changes occur in the Ti-containing fraction of the material. After pyrolysis at 700 °C, very small anatase and rutile crystallites are present. Further, inhomogeneities in the crystallite size and the crystalline polymorph arise at higher pyrolysis temperatures. Widespread conversion of TiO$_2$ to titanium oxycarbide occurs at 800 and 900 °C, alongside considerable growth of both anatase and rutile TiO$_2$. Since crystal growth and conversion to titanium oxycarbide is substantial for materials pyrolyzed at 900 °C, testing of the PF- and sucrose-TiO$_2$/C was restricted to samples pyrolyzed at 700 and 800 °C. Electrodes made from these composites (and cycled between 1 to 3 V vs Li/Li$^+$) have high capacities at low and moderate charge/discharge rates. During extended cycling at C/2, samples pyrolyzed at 700 °C have capacities that exceed 200 mAh/g. However, capacities decrease at high charge/discharge rates. While the exact origin of the increase in capacity requires further study, changing the voltage window to allow for Li$^+$ insertion/extraction into the 3DOM TiO$_2$/C is an effective means to substantially increase the Li$^+$ insertion/extraction capacity for these nanostructured electrodes. The capacities of the composite materials are greater than what can be obtained from similarly processed 3DOM C and compare favorably with other high-performing carbon and TiO$_2$ anode materials. In certain cases, the capacities of the 3DOM TiO$_2$/C match those of materials made using high cost, potentially toxic nanocarbon materials. Using a precursor with low toxicity, e.g., the one for sucrose-TiO$_2$/C, does not adversely affect capacities for Li$^+$ insertion/extraction. This finding opens up the possibility of tailoring various precursors for hard templated materials in order to achieve greener syntheses.

ASSOCIATED CONTENT

Ⓢ Supporting Information

Raman and FTIR analysis of the ammonium citratoperoxotitanate(IV) gel, Raman spectra, TEM images, SAED patterns, SAXS patterns, sorption isotherms, synthesis and characterization details for the 3DOM C reference material, cyclic voltammograms, and impedance spectroscopy data. This material is available free of charge via the Internet at http://pubs.acs.org.

AUTHOR INFORMATION

Corresponding Author
*A. Stein. Tel.: +1-612-624-1802. Fax: +1-612-626-7541. E-mail: a-stein@umn.edu.

Notes
The authors declare no competing financial interest.

REFERENCES

(1) Whittingham, M. S. Lithium Batteries and Cathode Materials. *Chem. Rev.* **2004**, *104*, 4271−4301.

(2) Lu, L.; Han, X.; Li, J.; Hua, J.; Ouyang, M. A Review on the Key Issues for Lithium-Ion Battery Management in Electric Vehicles. *J. Power Sources* **2013**, *226*, 272−288.

(3) Soloveichik, G. L. Battery Technologies for Large-Scale Stationary Energy Storage. *Annu. Rev. Chem. Biomol. Eng.* **2011**, *2*, 503−507.

(4) Scrosati, B.; Garche, J. Lithium Batteries: Status, Prospects and Future. *J. Power Sources* **2010**, *195*, 2419−2430.

(5) Goodenough, J. B.; Park, K.-S. The Li-Ion Rechargeable Battery: A Perspective. *J. Am. Chem. Soc.* **2013**, *135*, 1167−1176.

(6) Agubra, V.; Fergus, J. Lithium Ion Battery Anode Aging Mechanisms. *Materials* **2013**, *6*, 1310−1325.

(7) Verma, P.; Maire, P.; Novák, P. A Review of the Features and Analyses of the Solid Electrolyte Interphase in Li-Ion Batteries. *Electrochim. Acta* **2010**, *55*, 6332−6341.

(8) Chen, Z.; Belharouak, I.; Sun, Y.-K.; Amine, K. Titanium-based Anode Materials for Safe Lithium-Ion Batteries. *Adv. Funct. Mater.* **2013**, *23*, 959−969.

(9) Fröschl, T.; Hörmann, U.; Kubiak, P.; Kučerová, G.; Pfanzelt, M.; Weiss, C. K.; Behm, R. J.; Hüsing, N.; Kaiser, U.; Landfester, K.; Wohlfahrt-Mehrens, M. High Surface Area Crystalline Titanium Dioxide: Potential and Limits in Electrochemical Energy Storage and Catalysis. *Chem. Soc. Rev.* **2012**, *41*, 5313−5360.

(10) Ren, Y.; Liu, Z.; Pourpoint, F.; Armstrong, A. R.; Grey, C. P.; Bruce, P. G. Nanoparticulate TiO$_2$(B): An Anode for Lithium-Ion Batteries. *Angew. Chem., Int. Ed.* **2012**, *51*, 2164−2167.

(11) Kim, H.; Kim, M. G.; Cho, J. Unique Structural Changes of Three-Dimensionally Ordered Macroporous TiO$_2$ Electrode Materials During Electrochemical Cycling. *Adv. Energy Mater.* **2012**, *2*, 1425−1432.

(12) Guo, Y.-G.; Hu, Y.-S.; Sigle, W.; Maier, J. Superior Electrode Perfomance of Nanostructured Mesoporous TiO$_2$ (Anatase) through Efficient Hierarchical Mixed Conducting Networks. *Adv. Mater.* **2007**, *19*, 2087−2091.

(13) Yu, T.; Deng, Y. H.; Wang, L.; Liu, R. L.; Zhang, L. J.; Tu, B.; Zhao, D. Y. Ordered Mesoporous Nanocrystalline Titanium-Carbide/Carbon Composites from in Situ Carbothermal Reduction. *Adv. Mater.* **2007**, *19*, 2301−2306.

(14) Liu, R.; Ren, Y.; Shi, Y.; Zhang, F.; Zhang, L.; Tu, B.; Zhao, D. Controlled Synthesis of Ordered Mesoporous C-TiO$_2$ Nanocomposites with Crystalline Titania Frameworks from Organic-Inorganic-Amphiphilic Coassembly. *Chem. Mater.* **2008**, *20*, 1140−1146.

(15) Ishii, Y.; Kanamori, Y.; Kawashita, T.; Mukhopadhyay, I.; Kawaskai, S. Mesoporous Carbon-Titania Nanocomposites for High-Power Li-Ion Battery Anode Material. *J. Phys. Chem. Solids* **2010**, *71*, 511−514.

(16) Cheng, P.-Y.; Huang, C.-H.; Doong, R.-A. Ordered Mesoporous Carbon−TiO$_2$ Materials for Improved Electrochemical Performance of Lithium Ion Battery. *Carbon* **2012**, *50*, 4259−4268.

(17) Petkovich, N. D.; Rudisill, S. G.; Wilson, B. E.; Mukherjee, A.; Stein, A. Control of TiO$_2$ Grain Size and Positioning in Three-Dimensionally Ordered Macroporous TiO$_2$/C Composite Anodes for Lithium Ion Batteries. *Inorg. Chem.* **2014**, *53*, 1100−1112.

(18) Ma, J.; Xiang, D.; Li, Z.; Li, Q.; Wang, X.; Yin, L. TiO$_2$ Nanocrystal Embedded Ordered Mesoporous Carbons as Anode Materials for Lithium-Ion Batteries with Highly Reversible Capacity and Rate Performance. *CrystEngComm* **2013**, *15*, 6800−6807.

(19) Zeng, L.; Zheng, C.; Xia, L.; Wang, Y.; Wei, M. Ordered Mesoporous TiO$_2$-C Nanocomposites as an Anode Material for Long-Term Performance Lithium-Ion Batteries. *J. Mater. Chem. A* **2013**, *1*, 4293−4299.

(20) Huang, C.-H.; Gu, D.; Zhao, D.; Doong, R.-A. Direct Synthesis of Controllable Microstructures of Thermally Stable and Ordered Mesoporous Crystalline Titanium Oxides and Carbide/Carbon Composites. *Chem. Mater.* **2010**, *22*, 1760−1767.

(21) Zhou, D.-D.; Liu, H.-J.; Wang, Y.-G.; Wang, C.-X.; Xia, Y.-Y. Ordered Mesoporous/Microporous Carbon Sphere Arrays Derived from Chlorination of Mesoporous TiC/C Composite and Their Application for Supercapacitors. *J. Mater. Chem.* **2012**, *22*, 1937−1943.

(22) Zhang, C.; Zhang, Q.; Kang, S.; Li, X. A Novel Route for the Facile Synthesis of Hierarchically Porous TiO$_2$/Graphitic Carbon Microspheres for Lithium Ion Batteries. *J. Mater. Chem. A* **2014**, *2*, 2801−2806.

(23) Zhou, Y.; Kim, Y.; Jo, C.; Lee, J.; Lee, C. W.; Yoon, S. A Novel Mesoporous Carbon-Silica-Titania Nanocomposite as a High Perfomance Anode Material in Lithium Ion Batteries. *Chem. Commun.* **2011**, *47*, 4944−4946.

(24) Petkovich, N. D.; Stein, A. Controlling Macro- and Mesostructures with Hierarchical Porosity Through Combined Hard and Soft Templating. *Chem. Soc. Rev.* **2013**, *42*, 3721−3739.

(25) Petkovich, N. D.; Stein, A. Colloidal Crystal Templating Approaches to Materials with Hierarchical Porosity. In *Hierarchically Structured Porous Materials: From Nanoscience to Catalysis, Separation, Optics, Energy, and Life Science*; Su, B.-L., Sanchez, C., Yang, X.-Y., Eds.; Wiley-VCH Verlag GmbH & Co. KGaA: Weinheim, Germany, 2012; Vol. *1*, pp 55−129.

(26) Vu, A.; Qian, Y.; Stein, A. Porous Electrode Materials Lithium-Ion Batteries - How to Prepare Them and What Makes Them Special. *Adv. Energy Mater.* **2012**, *2*, 1056−1085.

(27) Jiang, H.; Yang, X.; Chen, C.; Zhu, Y.; Li, C. Facile and Controllable Fabrication of Three-Dimensionally Quasi-Ordered Macroporous TiO$_2$ for High Performance Lithium-Ion Battery Applications. *New J. Chem.* **2013**, *37*, 1578−1583.

(28) Jin, J.; Huang, S.-Z.; Liu, J.; Li, Y.; Chen, D.-S.; Wang, H.-E.; Yu, Y.; Chen, L.-H.; Su, B.-L. Design of New Anode Materials Based On Hierarchical, Three Dimensional Ordered Macro-Mesoporous TiO$_2$ for High Performance Lithium Ion Batteries. *J. Mater. Chem. A* **2014**, *2*, 9699−9708.

(29) Wang, H.; Yao, J. Use of Poly(furfuryl alcohol) in the Fabrication of Nanostructured Carbons and Nanocomposites. *Ind. Eng. Chem. Res.* **2006**, *45*, 6393−6404.

(30) Stein, A.; Wang, W.; Fierke, M. A. Functionalization of Porous Carbon Materials with Designed Pore Architecture. *Adv. Mater.* **2009**, *21*, 265−293.

(31) Yang, K.; Li, Y.; Tan, X.; Peng, R.; Liu, Z. Behavior and Toxicity of Graphene and Its Functionalized Derivatives in Biological Systems. *Small* **2013**, *9*, 1492−1503.

(32) Liu, Y.; Zhao, Y.; Sun, B.; Chen, C. Understanding the Toxicity of Carbon Nanotubes. *Acc. Chem. Res.* **2013**, *46*, 702−713.

(33) Schubert, U. Chemical Modification of Titanium Alkoxides for Sol-Gel Processing. *J. Mater. Chem.* **2005**, *15*, 3701−3715.

(34) Boettcher, S. W.; Bartl, M. H.; Hu, J. G.; Stucky, G. D. Structural Analysis of Hybrid Titania-Based Mesostructured Composites. *J. Am. Chem. Soc.* **2005**, *127*, 9721−9730.

(35) Kakihana, M.; Tada, M.; Shiro, M.; Petrykin, V.; Osada, M.; Nakamura, Y. Structure and Stability of Water Soluble (NH$_4$)$_8$[Ti$_4$(C$_6$H$_4$O$_7$)$_4$(O$_2$)$_4$]·8H$_2$O. *Inorg. Chem.* **2001**, *40*, 891−894.

(36) Josephson, D. P.; Popczun, E. J.; Stein, A. Effects of Integrated Carbon as a Light Absorber on the Coloration of Photonic Crystal-based Pigments. *J. Phys. Chem. C* **2013**, *117*, 13585−13592.

(37) Meng, Y.; Gu, D.; Zhang, F.; Shi, Y.; Yang, H.; Li, Z.; Yu, C.; Tu, B.; Zhao, D. Ordered Mesoporous Polymers and Homologous Carbon Frameworks Amphiphilic Surfactant Templating and Direct Transformation. *Angew. Chem., Int. Ed.* **2005**, *44*, 7053−7059.

(38) Fey, G. T.-K.; Kao, Y.-C. Synthesis and Characterization of Pyrolyzed Sugar Carbons under Nitrogen or Argon Atmospheres as Anode Materials for Lithium-Ion Batteries. *Mater. Chem. Phys.* **2002**, *73*, 37−46.

(39) Fierke, M. A.; Lai, C.-Z.; Bühlmann, P.; Stein, A. Effects of Architecture and Surface Chemistry of Three-Dimensionally Ordered Macroporous Carbon Solid Contacts on Performance of Ion-Selective Electrodes. *Anal. Chem.* **2010**, *82*, 680−688.

(40) Liu, G.; Liu, Y.; Wang, Z.; Liao, X.; Wu, S.; Zhang, W. F.; Jia, M. Direct Synthesis of Porous Carbon via Carbonizing Precursors of Aluminum Phosphate Containing Citric Acid. *Microporous Mesoporous Mater.* **2008**, *116*, 439−444.

(41) Zhang, H.; Banfield, J. F. Thermodynamic Analysis of Phase Stability of Nanocrystalline Titania. *J. Mater. Chem.* **1998**, *8*, 2073−2076.

(42) Shin, Y.; Li, X. S.; Wang, C.; Coleman, J. R.; Exarhos, G. J. Synthesis of Hierarchical Titanium Carbide from Titania-Coated Cellulose Paper. *Adv. Mater.* **2004**, *16*, 1212−1215.

(43) Koc, R. Kinetics and Phase Evolution During Carbothermal Synthesis of Titanium Carbide from Ultrafine Titania/Carbon Mixture. *J. Mater. Sci.* **1998**, *33*, 1049−1055.

(44) Bae, S.-T.; Shin, H.; Jung, H. S.; Hong, K. S. Synthesis of Titanium Carbide Nanoparticles with a High Specific Surface Area from a TiO$_2$ Core-Sucrose Shell Precursor. *J. Am. Ceram. Soc.* **2009**, *92*, 2512−2516.

(45) Hanaor, D. A. H.; Sorrell, C. C. Review of the Anatase to Rutile Phase Transformation. *J. Mater. Sci.* **2011**, *46*, 855−874.

(46) Zhang, W. F.; He, Y. L.; Zhang, M. S.; Yin, Z.; Chen, Q. Raman Scattering Study on Anatase TiO$_2$ Nanocrystals. *J. Phys. D: Appl. Phys.* **2000**, *33*, 912−916.

(47) Balachandran, U.; Eror, N. G. Raman Spectra of Titanium Dioxide. *J. Solid State Chem.* **1982**, *42*, 276−282.

(48) Klein, M. V.; Holy, J. A.; Williams, W. S. Raman Scattering Induced by Carbon Vacancies in TiC$_x$. *Phys. Rev. B* **1978**, *17*, 1546−1556.

(49) Lohse, B. H.; Calka, A.; Wexler, D. Raman Spectroscopy as a Tool to Study TiC Formation During Controlled Ball Milling. *J. Appl. Phys.* **2005**, *97*, 114912−114912-7 .

(50) Ferrari, A. C.; Robertson, J. Interpretation of Raman Spectra of Disordered and Amorphous Carbon. *Phys. Rev. B* **2000**, *61*, 14095−14107.

(51) Zhang, J.; Li, M.; Feng, Z.; Chen, J.; Li, C. UV Raman Spectroscopy Study on TiO$_2$. I. Phase Transformation at the Surface and in the Bulk. *J. Phys. Chem. B* **2006**, *110*, 927−935.

(52) Yin, H.; Wada, Y.; Kitamura, T.; Kambe, S.; Murasawa, S.; Mori, H.; Sakata, T.; Yanagida, S. Hydrothermal Synthesis of Nanosized Anatase and Rutile TiO$_2$ Using Amorphous Phase TiO$_2$. *J. Mater. Chem.* **2001**, *11*, 1694−1703.

(53) Shannon, R. D. Phase Transformation Studies in TiO$_2$ Supporting Different Defect Mechanisms in Vacuum-Reduced and Hydrogen-Reduced Rutile. *J. Appl. Phys.* **1964**, *35*, 3414−3416.

(54) Bücker, W. Preparation and DC Conductivity of an Amorphous Organic Semiconducting System. *J. Non-Cryst. Solids* **1973**, *12*, 115−128.

(55) Li, H.; Zhou, H. Enhancing the Performances of Li-Ion Batteries by Carbon-Coating: Present and Future. *Chem. Commun.* **2012**, *48*, 1201−1217.

(56) Yu, J.; Sushko, M. L.; Kerisit, S.; Rosso, K. M.; Liu, J. Kinetic Monte Carlo Study of Ambipolar Lithium Ion and Electron Polaron Diffusion into Nanostructured TiO$_2$. *J. Phys. Chem. Lett.* **2012**, *2*, 2076−2081.

(57) Huang, H.; Fang, J.; Xia, Y.; Tao, X.; Gan, Y.; Du, J.; Zhu, W.; Zhang, W. Construction of Sheet-Belt Hybrid Nanostructures from One-Dimensional Mesoporous $TiO_2(B)$ Nanobelts and Graphene Sheets for Advanced Lithiumm-Ion Batteries. *J. Mater. Chem. A* **2013**, *1*, 2495−2500.

(58) Zhao, B.; Jiang, S.; Su, C.; Cai, R.; Ran, R.; Tadé, M. O.; Shao, Z. A 3D Porous Architecture Composed of TiO_2 Nanotubes Connected with a Carbon Nanofiber Matrix for Fast Energy Storage. *J. Mater. Chem. A* **2013**, *1*, 12310−12320.

(59) Zhang, J.; Ni, J.; Guo, J.; Cao, B. TiO_2@C Composite Nanospheres with an Optimized Homogenous Structure for Lithium-Ion Batteries. *New J. Chem.* **2014**, *38*, 3722−3728.

(60) Xu, Y.; Guo, J.; Wang, C. Sponge-like Porous Carbon/Tin Composite Anode Materials for Lithium Ion Batteries. *J. Mater. Chem.* **2012**, *22*, 9562−9567.

(61) Peng, C.; Chen, B.; Qin, Y.; Yang, S.; Li, C.; Zuo, Y.; Liu, S.; Yang, J. Facile Ultrasonic Synthesis of CoO Quantum Dot/Graphene Nanosheet Composites with High Lithium Storage Capacity. *ACS Nano* **2012**, *6*, 1074−1081.

(62) Hao, Q.; Chen, L.; Xu, C. Facile Fabrication of a Three-Dimensional Cross-Linking TiO_2 Nanowire Network and Its Long-Term Cycling Life for Lithium Storage. *ACS Appl. Mater. Interfaces* **2014**, *6*, 10107−10112.

(63) Wagemaker, M.; Borghols, W. J. H.; Mulder, F. M. Large Impact of Particle Size on Insertion Reactions. A Case for Anatase Li_xTiO_2. *J. Am. Chem. Soc.* **2007**, *129*, 4323−4327.

(64) Milne, N. A.; Skyllas-Kazacos, M.; Luca, V. Crystallite Size Dependence of Lithium Intercalation into Nanocrystalline Rutile. *J. Phys. Chem. C* **2009**, *113*, 12983−12995.

(65) Borghols, W. J. H.; Wagemaker, M.; Lafont, U.; Kelder, E. M.; Mulder, F. M. Impact of Nanosizing on Lithiated Rutile TiO_2. *Chem. Mater.* **2008**, *20*, 2949−2955.

(66) Kubiak, P.; Pfanzelt, M.; Geserick, J.; Hörmann, U.; Hüsing, N.; Kaiser, U.; Wohlfahrt-Mehrens, M. Electrochemical Evaluation of Rutile TiO_2 Nanoparticles as Negative Electrode for Li-Ion Batteries. *J. Power Sources* **2009**, *194*, 1099−1104.

(67) Kaskhedikar, N. A.; Maier, J. Lithium Storage in Carbon Nanostructures. *Adv. Mater.* **2009**, *21*, 2664−2680.

(68) Pfanzelt, M.; Kubiak, P.; Wohlfahrt-Mehrens, M. Nanosized TiO_2 Rutile with High Capacity and Excellent Rate Capability. *Electrochem. Solid State Lett.* **2010**, *13*, A91−A94.

(69) Kang, D.-Y.; Kim, S.-O.; Chae, Y. J.; Lee, J. K.; Moon, J. H. Particulate Inverse Opal Carbon Electrodes for Lithium-Ion Batteries. *Langmuir* **2013**, *29*, 1192−1198.

(70) Wang, S.-X.; Yang, L.; Stubbs, L. P.; Li, X.; He, C. Lignin-Derived Fused Electrospun Carbon Fibrous Mats as High Performance Anode Materials for Lithium Ion Batteries. *ACS Appl. Mater. Interfaces* **2013**, *5*, 12275−12282.

(71) Guo, B.; Wang, X.; Fulvio, P. F.; Chi, M.; Mahurin, S. M.; Sun, X.-G.; Dai, S. Soft-Templated Mesoporous Carbon-Carbon Nanotube Composites for High Performance Lithium-Ion Batteries. *Adv. Mater.* **2011**, *23*, 4661−4666.

(72) Fan, Z.-J.; Yan, J.; Wei, T.; Ning, G.-Q.; Zhi, L.-J.; Liu, J.-C.; Cao, D.-X.; Wang, G.-L.; Wei, F. Nanographene-Constructed Carbon Nanofibers Grown on Graphene Sheets by Chemical Vapor Deposition: High-Performance Anode Materials for Lithium Ion Batteries. *ACS Nano* **2011**, *5*, 2787−2794.

(73) Jamink, J.; Gaberscek, M. Li Ion Migration at the Interfaces. *MRS Bull.* **2009**, *34*, 942−948.